Turbulent Aeroheating Measurements on a 7-deg Half-Angle Cone in a High-Enthalpy CO_2 Expansion Tunnel

Brian R. Hollis*

NASA Langley Research Center, Hampton, VA 23681

Michael D. Barnhardt†

NASA Ames Research Center, Moffett Field, CA 94035

Matthew Maclean‡, Aaron Dufrene§, and Tim Wadhams**

Calspan-University at Buffalo Research Center, Buffalo, NY, 14225

A database of heating and pressure measurements on a 7-deg half-angle cone in a high-enthalpy expansion tunnel in CO_2 has been generated to support development and validation of computational models to be employed in the design of future Mars missions. Laminar, transitional, and turbulent simulations were performed at the test conditions for comparisons with the data. Close agreement was obtained for both fully-laminar and fully-turbulent conditions. For the remaining transitional/turbulent conditions, agreement to within, or slightly more than, the estimated experimental uncertainty was demonstrated. The influence of transition intermittency and transition length models on predicted heating levels was demonstrated, as were differences in turbulent heating predictions generated using various algebraic, one-equation, and two-equation turbulence models. These comparisons provide some measure of confidence in turbulent simulation capabilities; however, because the data were not obtained on a relevant entry vehicle geometry, it is not

* Associate Fellow AIAA, Senior Technical Lead, Aerothermodynamics Branch, Research Directorate

† Senior Member AIAA, Research Scientist, Aerothermodynamics Branch, Entry Systems and Technology Division

‡ Senior Member AIAA, Senior Research Scientist, Aerosciences Group

§ Senior Member AIAA, Senior Research Scientist, Aerosciences Group

** Senior Member AIAA, Senior Research Scientist, Aerosciences Group

possible to fully quantify computational uncertainties for the definition of Mars mission aerothermodynamic environments at this time

Nomenclature

H_0 = total enthalpy (J/kg)

H_w = wall enthalpy (J/kg)

L = model length (m)

M_∞ = free stream Mach number

p_w = pressure at the wall (Pa)

p_∞ = free stream pressure (Pa)

q_w = heat-transfer rate at the wall (W/m^2)

$Re_{\infty,L}$ = free stream Reynolds number based on model length

R_N = model nose radius (mm)

T_∞ = free stream temperature (K)

T_w = wall temperature (K)

U_∞ = free stream velocity (m/s)

x = distance from virtual nosetip (m)

μ_∞ = free stream viscosity (kg/m.s)

ρ_∞ = free stream density (kg/m^3)

I. Background and Introduction

While NASA has a long history of Mars exploration, missions to-date have all been performed using relatively small robotic orbiters and/or landers, whereas future missions under consideration, including sample return and human exploration, will require new vehicle architectures with greater performance requirements. Among the requirements identified by systems analysis studies (e.g., [1-4]) for future Mars missions are an order-of-magnitude increase in payload landing mass (currently < 1 t), an order-of–magnitude reduction in landing footprint (currently > 10 km), and an order-of-magnitude reduction in aerothermodynamic environment margins (currently > 50%) for Thermal Protection System (TPS), where the state-of-the-art for these requirements is based on those developed for the Mars Science Laboratory mission [5-6].

One of the key enablers for meeting these requirements is the validation and improvement of Computational Fluid Dynamics (CFD) tools used in the simulation of Entry, Descent and Landing (EDL) on Mars. These tools provide the aerodynamic and aeroheating environments used in the design of an EDL system. As sources of flight data have been very limited until the Mars Science Laboratory (MSL) mission [7] with its MEDLI (Mars Science Laboratory Entry, Descent and Landing Instrumentation) instrumentation suite, validation efforts for CFD tools have primarily relied on comparisons to experimental ground test data. However, as shown in a survey of Mars-relevant ground tests [8], there are large differences between the experimental data and numerical predictions and these differences are attributable, at least in part, to the quality of the ground test data.

To address the lack of high-fidelity ground test data, a test program has been conducted to obtain high-enthalpy CO_2 aerothermodynamic data in the Calspan-University at Buffalo Research Center (CUBRC) LENS-XX Expansion Tunnel. The selection of the LENS-XX Expansion Tunnel for this test program addresses one of the key deficiencies identified in the survey of historical data sets (as discussed in [8]), which is the undefined, but presumably large, uncertainty in free stream conditions owing to nonequilibrium vibrational and/or chemical excitation produced by the operational mode of reflected shock tunnels. This uncertainty mostly can be eliminated through testing in an expansion tunnel environment, in which higher velocities are produced through unsteady expansion into a low pressure section, rather than by processing the flow through a reflected shock.

In the first part of the program, a 70-deg sphere-cone heat shield design similar to the MSL entry vehicle was tested across a wide range of densities and velocities. Surface convective and radiative heat-transfer data and pressure data were obtained through an instrumentation suite consisting of platinum thin-film gauges, chromel-constantan coaxial thermocouples, piezoelectric pressure transducers, and radiometers. Flow field shock-shape imagery was also generated through schlieren photography. These data were compared to CFD simulations performed at the test conditions in order to better define uncertainties for NASA computational tools and the results were presented in [9-11].

The outstanding issue from the 70-deg sphere-cone study was the lack of turbulent data for code validation. The free stream conditions necessary for turbulent flow over this MSL geometry were at the limits of the facility operational range. While transitional/turbulent data were obtained, the quality of some of the data was questionable and the overall results were inconclusive with respect to validation of CFD turbulence modeling. In order to attempt to address this problem, the second part of the test program was conducted using a 1.12 m long, 7-deg half-

angle cone geometry. Surface heating and pressure measurements were performed at enthalpies of 4 to 12 MJ/kg in CO_2 across a range of laminar, transitional, tripped, and turbulent conditions. These data and comparisons with CFD predictions are presented herein.

II. Experimental Method

A. LENS XX Expansion Tunnel

The CUBRC LENS-XX Expansion Tunnel facility generates test flows in a unique manner that is very different from other high-enthalpy facility types. The expansion tunnel consists of three shock-tube segments that are filled with: (1) a low-molecular weight driver gas (hydrogen or helium), (2) the test gas (in this case, carbon dioxide), and (3) a low-pressure accelerator gas (air or hydrogen). Conditions in the three segments of the facility are tailored to process the test gas through two unsteady processes to achieve a target test condition. The test gas is first set into motion by rupture of the primary diaphragm that separates the first and second segments to produce an unsteady, traveling shock of weak to moderate strength. This shock ruptures the secondary diaphragm that separates the second and third segments, causing the test gas to be processed through an unsteady acceleration to increase its velocity. The moving test gas is contained between a leading contact surface with the acceleration gas and a trailing unsteady expansion fan, resulting in test durations over the model on the order of one millisecond.

The unique benefit of the expansion tunnel mode of operation is that the majority of the total enthalpy in the test gas is added as kinetic energy directly by the unsteady expansion process, rather than through a shock reflection. Since the free stream gas is not stagnated before it reaches the test article, the peak thermal temperature of the flow is substantially lower than it is for other high enthalpy facilities that expand from a stagnant reservoir. As a result, the expansion tunnel free stream flow is generally not subject to the nonequilibrium chemical and vibrational excitation present in reflected shock tunnels, greatly reducing the uncertainties in specification of the test conditions. Additional description of the LENS-XX expansion tunnel and blunt body data collected during recent experimental programs can be found in Refs. [12-14].

B. Determination of Test Conditions

Test conditions in LENS-XX were computed using the CHEETAh (CUBRC High Enthalpy Expansion Tunnel Analysis) code [15]. This code solves for the intermediate states of the primary and secondary wave systems incorporating equilibrium chemistry, ionization, and thermodynamic excitation mechanisms. It also can incorporate

measured, as-run data from the facility for each shot to anchor the calculations, including shock wave speeds, Pitot and/or static pressure, and free stream velocity.

C. Model Geometry and Instrumentation

The model (Figure 1) was a 7-deg half-angle cone with a total axial length of L =1.12 m and interchangeable nose tips of different radii. For this test program, two different nose radii were used: a nominally sharp nose (R_N ~0.17 mm), and a blunt nose (R_N = 2.5 mm). The model was instrumented with 32 thin-film heat-transfer gauges and 18 piezoelectric pressure gauges.

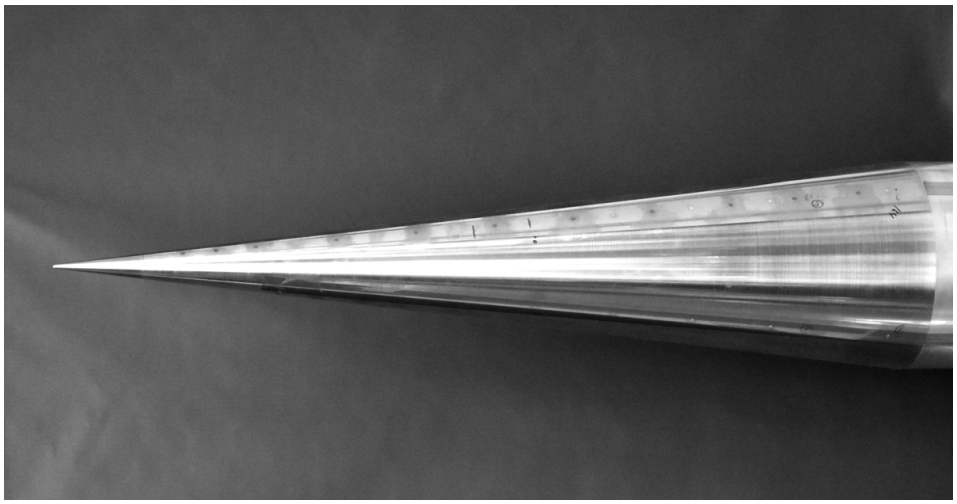

Figure 1. 7-deg half-angle cone model.

D. Uncertainty Analysis

CUBRC provides a general uncertainty analysis for each sensor type (surface pressure, thin-film, and thermocouple) to obtain nominal uncertainties of ±6%, ±9% and ±13%, respectively. These values represent root-sum-squared combination of uncertainties due to instrumentation calibration, signal collection, substrate material properties (used in heat-transfer data reduction), flow field pressure and velocity fluctuations, and the "stagnation heating augmentation" phenomena observed in numerous blunt body heating studies [16]. This analysis provides nominal values for general discussion of uncertainties.

An additional analysis has also been performed to disambiguate the traceable instrumentation uncertainties from flow-field uncertainties that rely on estimates of fluctuations (and the stagnation augmentation phenomena) and are applied uniformly to all shots. These "instrumentation-only" uncertainties are then determined as per Table 1.

Next, a run-specific and sensor-specific uncertainty is added to these instrumentation-only values. The root-mean-square (RMS) deviation of each individual sensor over the time-averaging data acquisition window is computed and these values are then added to the instrumentation-only uncertainty through a root-sum-square calculation. This RMS component accounts for two uncertainty sources: the effects of flow-field fluctuations over the data-averaging period and any degradation of individual sensor performance over the course of the test program. These "sensor-specific" values will be used to denote uncertainties on data plots in the Analysis and Results section. As these values varied from run to run and from sensor to sensor, it is not possible to provide a single value to represent sensor-specific uncertainties for each sensor as it was for the nominal uncertainties presented at the beginning of this section.

Table 1. Instrumentation-Only Uncertainties

	Pressure	**Thin-film**	**Thermocouple**
Instrument Calibration	±0.6%	±0.22%	±5%
Signal Collection and Processing	±2%	±2%	±2%
Substrate Material Properties	N/A	±2.5%	N/A
Instrumentation Only Root-Sum-Square	**±2.1%**	**±3.2%**	**±5.4%**

III. Computational Methods

A. Flow Field Solvers

Flow field computations were performed at the test conditions using the NASA LAURA (Langley Upwind Aerothermodynamic Relaxation Algorithm) and DPLR (Data-Parallel Line Relaxation) codes [17, 18]. These codes represent the current NASA state-of-the-art for Navier-Stokes simulations of chemically reacting hypersonic flows and have been used extensively in the design of all NASA Mars missions since Mars Pathfinder. Both codes are structured, three-dimensional, finite-volume solvers with nonequilibrium chemical and vibrational modeling capabilities. For simulation of the LENS-XX test conditions, a 5-species (CO_2, CO, O_2, C, and O) model with an isothermal cold-wall (T_w = 300 K) was used. Kinetic reaction rates for these species are provided in Ref. [11].

B. Turbulence and Transition Modeling

Depending on test conditions, laminar or turbulent flowfield models were employed. The baseline method for turbulence simulations was the algebraic Baldwin-Lomax model [19]. For comparison purposes, selected cases were also run using the algebraic Cebeci-Smith model [20], one-equation Spalart-Allmaras model [21, 0], and two-equation Wilcox k-ω model [22]. The Dhawan-Narsimha transition definition was used with the algebraic turbulence models.

An algebraic turbulence model was selected as the baseline because of the importance of such models to current NASA mission design processes. Algebraic models have been proven to be fast, stable, and accurate in the prediction of turbulent attached flows such as on the forebody aeroshell of an entry vehicle. Algebraic models were the design standard for both the MSL entry vehicle and Orion crew capsule aeroshell heating environments. The accuracy of these models has been demonstrated for perfect-gas turbulent conditions for these vehicles through extensive comparisons with experimental data [23, 24]. The lack of validation data for turbulent reacting CO_2 environments was, as noted, the motivation for the current study.

Transition modeling is a related, but separate, issue from turbulence modeling and is dependent on vehicle configuration, free stream conditions (including noise) and surface roughness. However, for NASA missions such as Orion and MSL, transition has not been a major issue. For both vehicles, which feature large aeroshells flying at high angles of attack, transition was expected to occur very early in the flight trajectory, well before the peak heating trajectory point. Therefore, the heat shields for these vehicles were designed to fully-turbulent levels throughout their trajectories. The benefits of attempting to precisely define the transition onset point were outweighed by the uncertainties inherent in transition modeling and the minimal mass savings that inclusion of a transition model would have provided to the vehicle design. Because of these factors, prediction of the transition onset location was not a goal in the current study, and instead, transition onset with the algebraic models was simply specified to occur at the location determined from the test data. For the one and two equation models, transition was not specified and the evolution of turbulence was a function of the respective model.

C. Radiation Transport and Surface Catalysis Models

While shock-layer radiation and surface catalysis modeling showed significant impact at some conditions during the first phase (testing of the MSL geometry) of this test program [11], enthalpy levels for this second phase were low enough that these phenomena could be neglected. Therefore, radiation was not included in the simulations. The

wind tunnel model surface boundary condition was set as fully-catalytic to O_2 recombination and noncatalytic for other reactions, although no differences in predicted heating were observed between noncatalytic and fully-catalytic solutions at the enthalpies of this test.

IV. Results and Analysis

A. Overview of Test Conditions

Surface heat transfer and pressure data were obtained from 13 shots performed in the LENS-XX Expansion Tunnel. Owing to the length of the model, schlieren images were not obtained because only a small section of the model was visible through the test section window. Nine shots were performed with the sharp (0.17 mm) nose and four shots were made with the blunt (2.5 mm) nose. Laminar, transitional, or turbulent flow was generated depending on the test condition and nose radius. Additionally, boundary-layer trips were employed in several shots to ensure that fully-turbulent flow was generated at a precise location (30 cm from the nose). Conditions for the shots are listed in Table 2, ordered by nose radius and Reynolds number, and the state of the boundary layer is also noted. All runs were performed at zero deg. angle of attack at an isothermal 300K wall temperature. A velocity-density map of the test conditions for both this test and the previous 70-deg sphere-cone test is given in Figure 2.

Table 2. Test conditions.

Shot	R_n (mm)	M_∞	U_∞ (m/s)	T_∞ (K)	ρ_∞ [illegible]	P_∞ (Pa)	$Re_{\infty,L}$	H_0- H_w (J/kg)	[CO_2]	Trip height (mm)	Boundary-layer state
5	0.17	8.76	2905	472	1.358E-02	1212	1.989E+06	4.390E+06	1.00	n/a	transitional
7	0.17	10.70	4134	659	1.583E-02	1969	2.539E+06	8.900E+06	1.00	n/a	transitional
9	0.17	10.30	3255	422	1.410E-02	1125	2.540E+06	5.410E+06	1.00	n/a	transitional/turbulent
12	0.17	9.65	3542	587	3.788E-02	4204	5.683E+06	6.560E+06	1.00	n/a	transitional/turbulent
11	0.17	9.88	2600	283	6.480E-02	3464	1.332E+07	3.370E+06	1.00	n/a	turbulent
18	0.17	9.70	4783	1093	1.146E-02	2365	1.486E+06	1.230E+07	1.00	0.889	tripped/transitional
19	0.17	10.00	4028	713	1.571E-02	2117	2.314E+06	8.540E+06	1.00	0.889	tripped/turbulent
14	0.17	10.30	3887	617	1.930E-02	2245	3.060E+06	7.870E+06	1.00	0.889	tripped/turbulent
13	0.17	9.96	3114	414	3.172E-02	2483	5.551E+06	4.960E+06	1.00	0.635	tripped/turbulent
6	2.50	11.50	3216	325	4.210E-03	259	9.417E+05	5.200E+06	1.00	n/a	laminar

2	2.50	9.99	3247	452	1.863E-02	1589	3.161E+06	5.420E+06	1.00	n/a	transitional
4	2.50	9.59	3200	478	3.798E-02	3433	6.064E+06	5.290E+06	1.00	n/a	transitional/turbulent
17	2.50	10.60	3953	606	1.700E-02	1946	2.779E+06	8.120E+06	1.00	1.143	tripped/turbulent

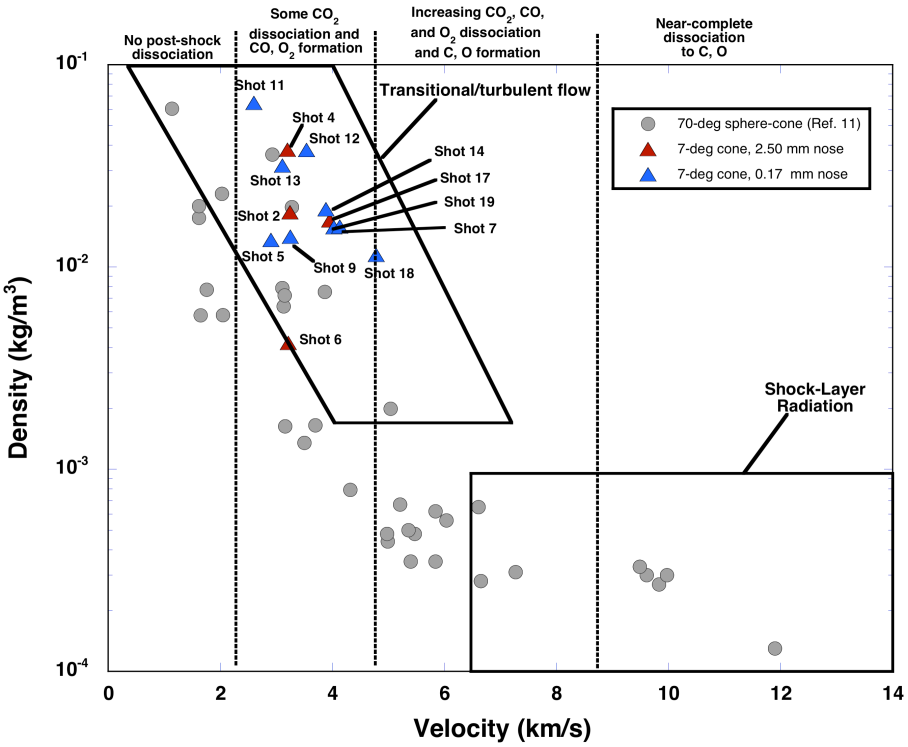

Figure 2. Velocity vs. density map of test conditions.

B. Comparisons Between Experimental Data and Baseline Predictions

In this section, baseline comparisons between data and predictions for surface heating and pressure distributions will be presented. Sharp nose (R_N = 0.17 mm) comparisons for cases without boundary-layer trips are presented in Figure 3 through Figure 7 and for cases with trips in Figure 8 through Figure 11. Blunt nose (R_N = 2.50 mm) comparisons for cases without trips are presented in Figure 12 through Figure 14 and the single blunt nose case with trips is shown in Figure 15. For each group of comparisons, the figures are ordered in terms of increasing Reynolds number. Error bars in the figures are based on the shot-specific root-sum-square of instrumentation uncertainty and temporal variation (as per Section II-D). It is notable that the heat-flux uncertainties were larger in the transition region between laminar and turbulent flow owing to the fluctuating nature of the flow field during transition.

Computational solutions in this section were performed at the nominal test conditions based on the CHEETah analysis (Section II-B) using LAURA and DPLR (Section III-A) to generate laminar and turbulent solutions. The algebraic Baldwin-Lomax model was used for all solutions presented in this section, with the transition onset location set to the observed experimental location. For natural transition cases, the transition length was set to the running length from the nose to transition onset, and for artificially tripped cases, the transition length was set to zero.

For those cases with significant length of laminar flow – sharp nose shot 5 (Figure 3), shot 7 (Figure 4), shot 18 (Figure 8), and blunt nose shot 6 (Figure 12) and shot 2 (Figure 13) – the agreement between predictions and measurements of heat transfer rates in the laminar region was well within the experimental uncertainty. This observation is consistent with results from the Group 1 and Group 3 (laminar, nonreacting to slightly dissociating) cases from the prior 70-deg sphere test program [11]. The fidelity of pressure predictions is more difficult to assess owing to the sparseness of pressure instrumentation. There were four pressure gauges spaced around the circumference of the model at both of the measurement locations, and for several cases, the scatter between gauges was larger than the estimated experimental uncertainty. One interesting observation for the transitional simulations is the slight increase in predicted surface pressures downstream of the transition location.

Natural transition was observed for sharp nose shot 5 (Figure 3), shot 7 (Figure 4), shot 9 (Figure 5) and shot 12 (Figure 6), and for blunt nose shot 2 (Figure 13) and shot 4 (Figure 14). As a reminder, the goal of this study was to assess the performance of computational tools in the prediction of turbulent heating levels, not to develop or assess transition correlations or models. As such, boundary-layer transition locations for the simulations were taken from the data set. Of these natural transition cases, only sharp nose shots 9 and 12 and blunt nose shot 4 free stream conditions produced sufficient running length downstream of transition onset for a fully-turbulent boundary layer to develop. Turbulent heating predictions for shots 9 and 4 fell within the estimated experimental uncertainty, while predictions for shot 12 slightly exceeded the uncertainty range. For the remaining transitional shots, the transitional/turbulent heating predictions were in at least qualitative agreement with the data, but no attempt was made to refine the transition modeling to produce better agreement.

Boundary-layer trips were employed with the intent of producing fully-turbulent flow with zero-length transition for sharp nose shot 18 (Figure 8), shot 19 (Figure 9), shot 14 (Figure 10) and shot 13 (Figure 11) and blunt nose shot 17 (Figure 15). For these cases, zero-length transition was specified at the x = 30 cm trip location. The trips were

ineffective for shot 18 and marginally effective for shot 17, so these two cases were not well suited for comparisons. For the remaining shots 19, 14, and 13, the predictions were consistently higher than the data. For shot 19, LAURA and DPLR predictions fell within the experimental uncertainty range, while for shots 14 and 13, the predictions were slightly outside the upper uncertainty bounds, with the DPLR predictions being slightly lower, and closer to the data than the LAURA predictions.

A single case of fully-turbulent flow via natural transition was obtained for shot 11 (Figure 7). For this case, both LAURA and DPLR turbulent heating predictions were slightly higher than, but within the experimental uncertainty range of, the majority of the data points.

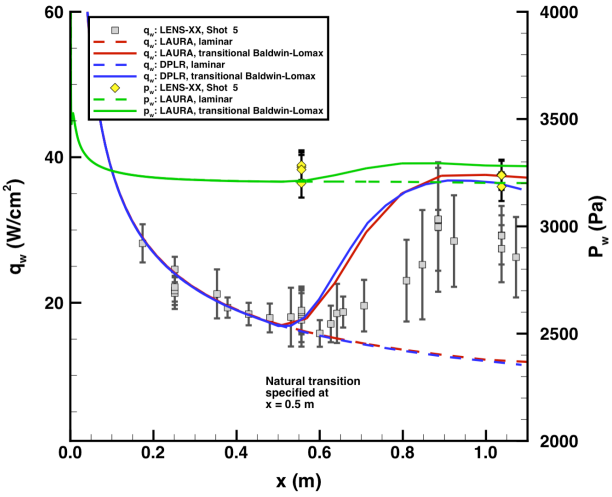

Figure 3. Shot 5 data comparison with predictions, sharp nose, $Re_{\infty,L}$=1.99×10^6.

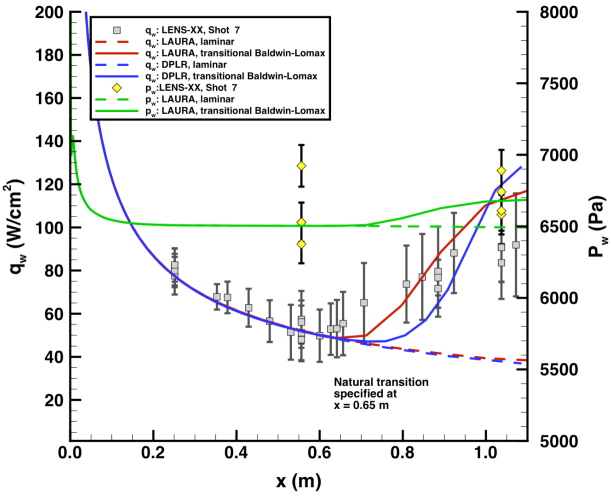

Figure 4. Shot 7 data comparison with predictions, sharp nose, $Re_{\infty,L}$=2.54×10^6.

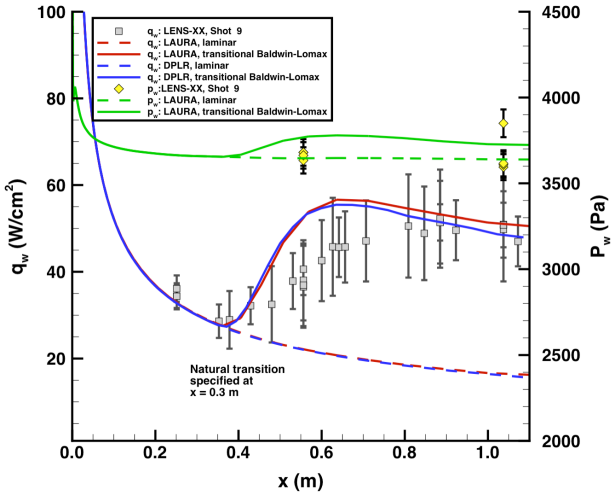

Figure 5. Shot 9 data comparison with predictions, sharp nose, $Re_{\infty,L}=2.54\times10^6$.

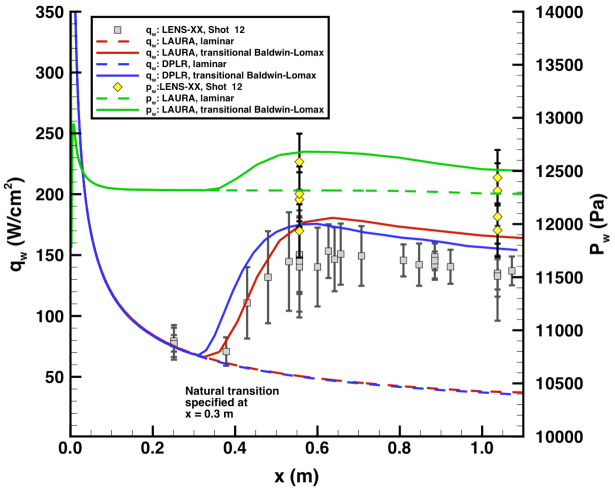

Figure 6. Shot 12 data comparison with predictions, sharp nose, $Re_{\infty,L}=5.68\times10^6$.

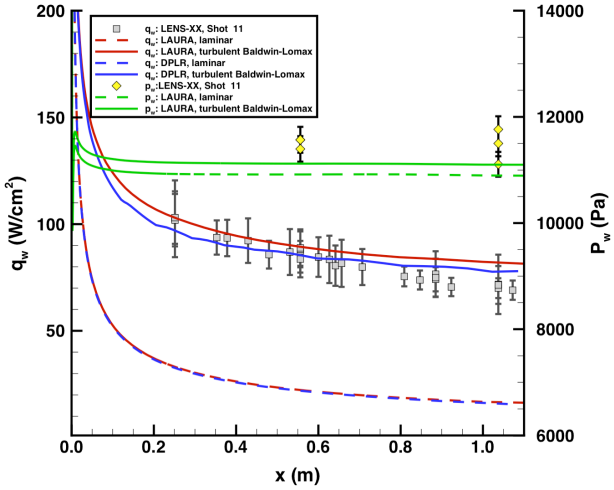

Figure 7. Shot 11 data comparison with predictions, sharp nose, $Re_{\infty,L}=13.3\times10^6$.

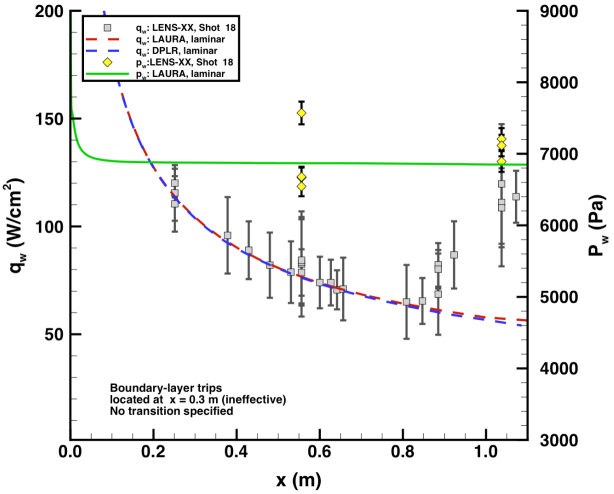

Figure 8. Shot 18 data comparison with predictions, sharp nose with trips, $Re_{\infty,L}=1.49\times10^6$.

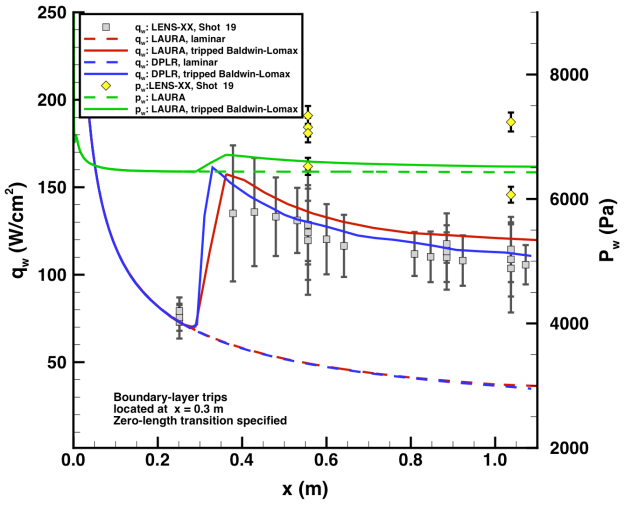

Figure 9. Shot 19 data comparison with predictions, sharp nose with trips, $Re_{\infty,L}=2.31\times10^6$.

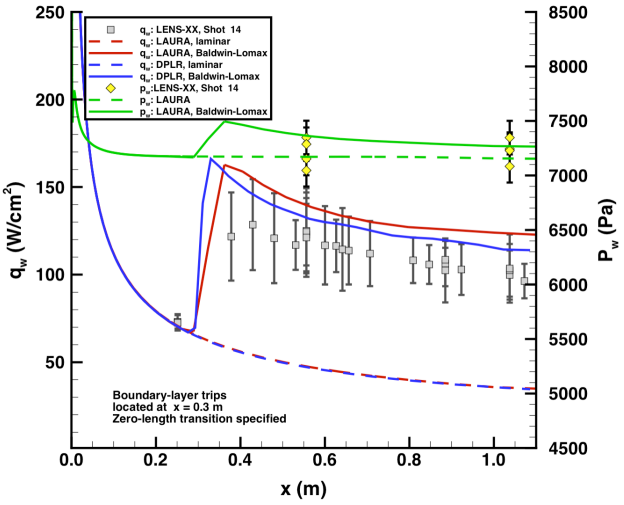

Figure 10. Shot 14 data comparison with predictions, sharp nose with trips, $Re_{\infty,L}=3.06\times10^6$

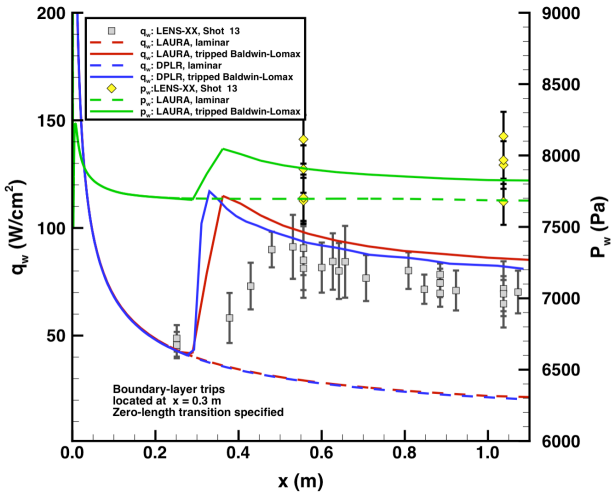

Figure 11. Shot 13 data comparison with predictions, sharp nose with trips, $Re_{\infty,L}=5.55\times10^6$.

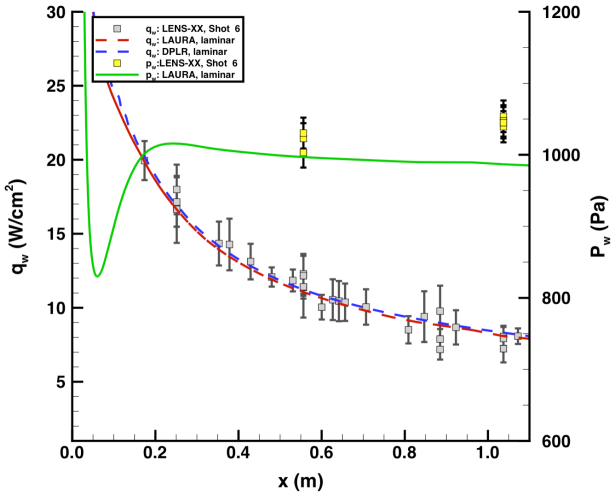

Figure 12. Shot 6 data comparison with predictions, blunt nose, $Re_{\infty,L}$=0.94×10^6.

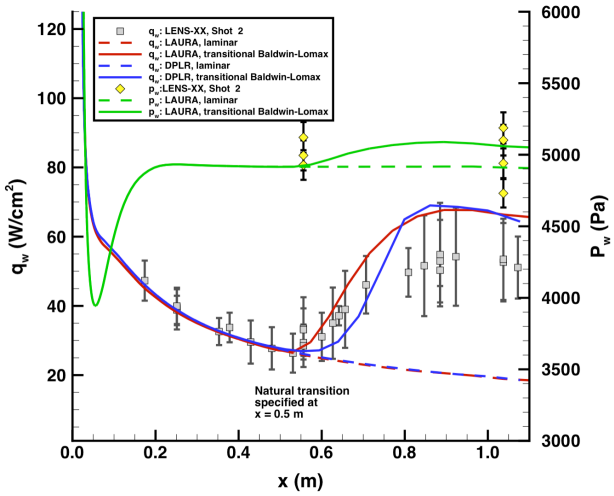

Figure 13. Shot 2 data comparison with predictions, blunt nose, $Re_{\infty,L}$=3.16×10^6.

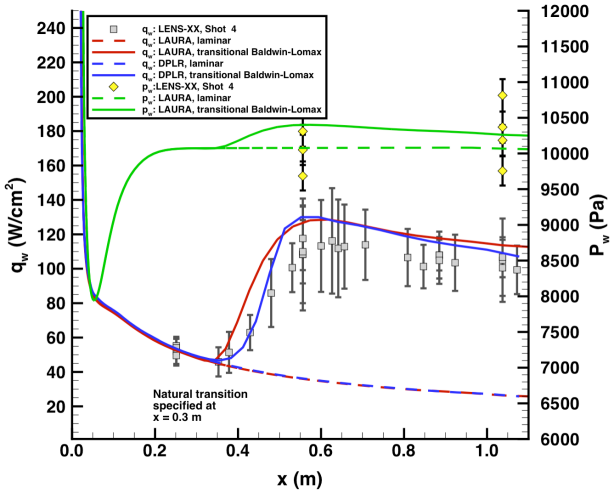

Figure 14. Shot 4 data comparison with predictions, blunt nose, $Re_{\infty,L}$=6.06×10^6.

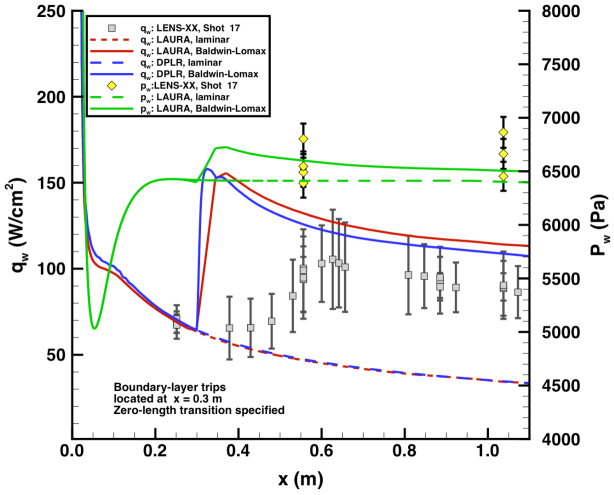

Figure 15. Shot 17 data comparison with predictions, blunt nose with trips, $Re_{\infty,L}$=2.79×10^6.

C. Effects of Transition Model on Predicted Heating Levels

Although transition modeling was not the focus of this study, shots 2 and 4 (sharp nose with natural transition) were used as a test case to demonstrate the effects of the transition intermittency model function and transition length in heating predictions. In Figure 16, the effects of transition length on heating predictions is illustrated by varying the transition length from one-half to two times the baseline transition length, which was set to the running

length from the nose to the transition onset location (50 cm for this case). Although the impact of length variation is clear in the transition region, heating levels for all lengths approached convergence downstream of transition. In Figure 17, the effects of the transition intermittency model are shown through use of an exponential function (as per Dhawan –Narasimha [25]), a sigmoid function, and a hyperbolic tangent function. Downstream of transition, all models produced the same heating levels, but the shape of the distribution in the transition region varied. The hyperbolic tangent produced the shortest transition length and the sigmoid function produced the longest transition length.

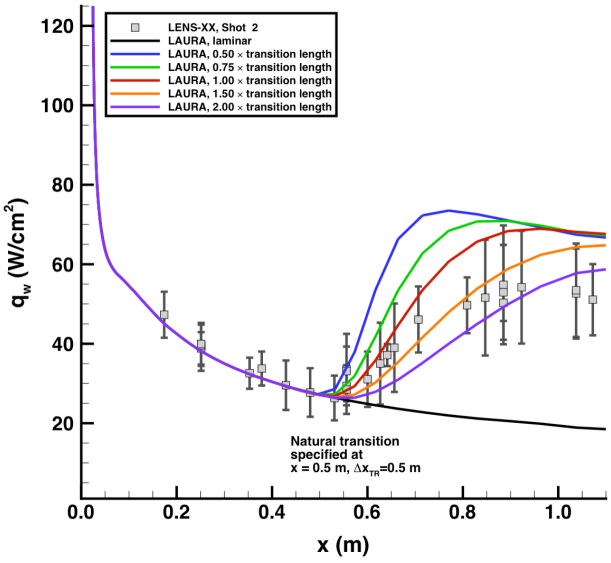

Figure 16. Shot 2 transition length effects.

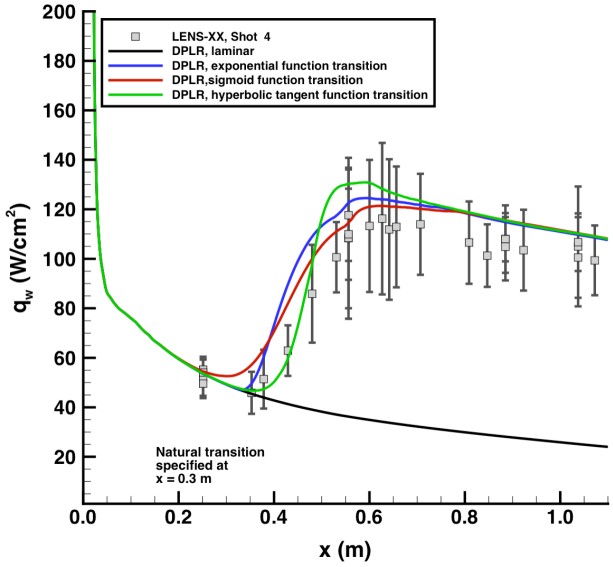

Figure 17. Shot 4 transition model effects.

D. Effects of Turbulence Model on Predicted Heating Levels

As noted previously, the algebraic Baldwin-Lomax model was employed as the baseline method for comparison in this study because of its application to NASA flight projects, i.e., the MSL and Orion entry vehicles. However, to demonstrate the effects of the turbulence model on predicting heating, solutions were generated for shot 11 (Figure 18) and shot 4 (Figure 19) using the algebraic Cebeci-Smith model, one-equation Spalart-Allmaras model, and two-equation Wilcox *k*-ω model. While the one- and two-equation models predicted transition at different locations, both from each other and from the measured location, the predicted heating levels from all models converged

downstream from the transition region. Although all models essentially agreed in the turbulent region, it is worth noting that the two-equation solution required an order of magnitude greater computational time to reach convergence than the algebraic and one-equation solutions, and it also demonstrated numerical stability issues.

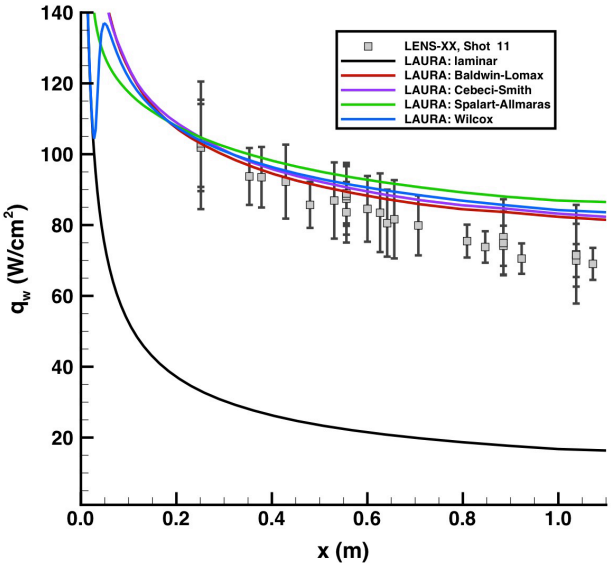

Figure 18. Shot 11 turbulence model effects.

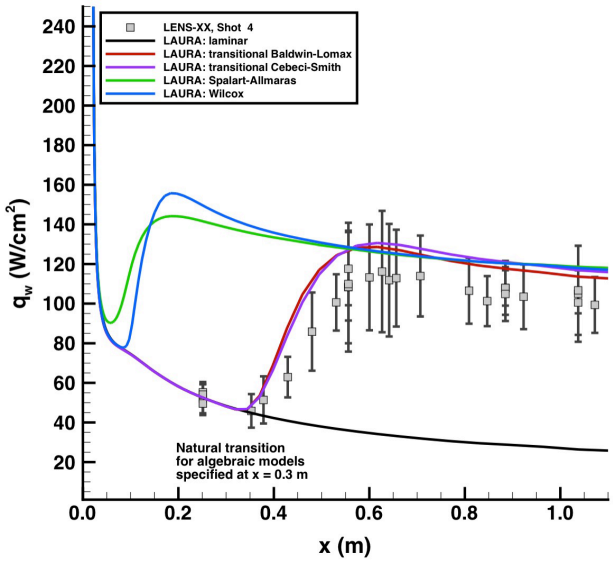

Figure 19. Shot 4 turbulence model effects.

E. Blunt Body Turbulent Heating Augmentation Problem

Although these 7-deg half-angle cone comparisons were reasonably successful, they do not provide data on configurations of interest for current NASA exploration missions, i.e. blunt body geometries. It is thus worthwhile to briefly survey some of the existing blunt-body turbulent heating comparisons to highlight this issue. Turbulent aeroheating data on the MSL geometry has been obtained in both the Arnold Engineering Development Center Tunnel 9 [24] in perfect gas N_2 and the CUBRC LENS-XX facility in CO_2 [11]. Sample comparisons between measurements and predictions for these test programs are shown in Figure 20 and Figure 21, respectively.

In both cases, fully-turbulent flow was produced on the leeward side of the aeroshell ($z > 0$). For the AEDC Tunnel 9 example (and all the other turbulent data from that test program), good comparisons were demonstrated between the data and both the Baldwin-Lomax and Cebeci-Smith turbulent predictions. However, the same agreement was not evident in the CUBRC test program. The Baldwin-Lomax model predictions provided the best agreements with the data, especially in the growth of the turbulent heating levels toward the leeward side shoulder. However, while the Spalart-Allmaras model predictions showed the same growth trend, the heating magnitude was

lower than predicted by Baldwin-Lomax, whereas the Cebeci-Smith model predictions showed essentially constant turbulent heating levels on the leeward side. Similar discrepancies between turbulent model predictions were observed for MSL flight environment computations [26], in this case between Baldwin-Lomax and two-equation Shear Stress Transport (SST) models.

It would be tempting to declare the Baldwin-Lomax model as "correct" for high-enthalpy, attached flow conditions based on the LENS XX comparisons for MSL. However, as noted in [11], the turbulent heating data obtained in LENS-XX were not considered to be of validation quality due to discrepancies in data between various runs, as well as the fact that most of the shots produced "transitional" rather than "fully-turbulent" boundary layers. Therefore, until additional, validation quality turbulent data can be obtained on mission-relevant geometries, uncertainties in blunt body turbulent predictions in high-enthalpy CO_2 cannot be fully quantified.

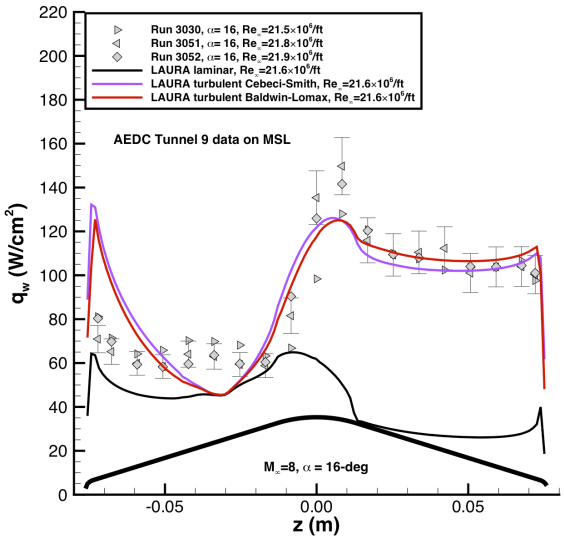

Figure 20. MSL turbulent comparisons from AEDC Tunnel 9 in perfect-gas N_2.

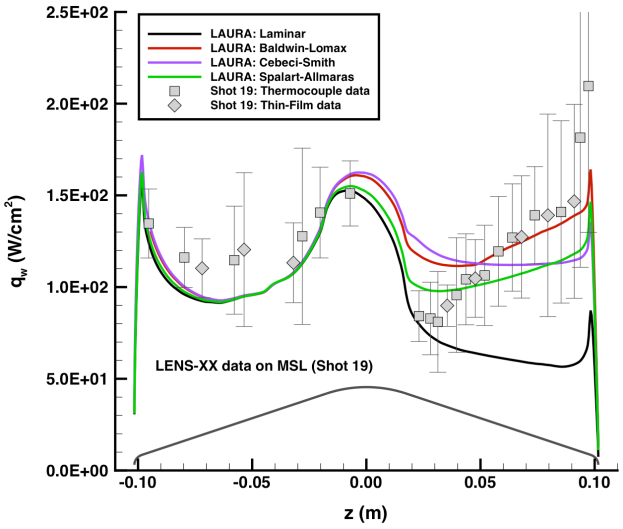

Figure 21. MSL turbulent comparisons from CUBRC LENS-XX in reacting CO_2.

V. Summary and Conclusions

A test series was conducted on a 7-deg half-angle cone in a high-enthalpy CO_2 environment to obtain laminar, transitional, and turbulent heating data for code validation. Comparisons between measured data and computational predictions from two codes using several different turbulence models have been shown. Agreement for heat-transfer rates to within the experimental uncertainty was demonstrated for the single fully-laminar and naturally fully-

turbulent test points. For the remaining test points, the flow was either naturally transitional or it was artificially tripped at ~ 30 cm from the cone tip. Depending on the specific test conditions, the boundary layer either remained transitional or reached a fully-turbulent state before the end of the cone. For those transitional cases that resulted in turbulent flow, turbulent heating predictions from both codes were higher than the data. In some cases, the predictions fell within the experimental uncertainty bounds and in other cases the predictions were slightly beyond the upper uncertainty bounds.

The comparisons in this study of transitional/turbulent data with predictions provide a necessary, but not sufficient validation of computational turbulence modeling for high-enthalpy CO_2 flows. While these heat-transfer comparisons were reasonably good (agreement to within or slightly greater than estimated experimental uncertainties), they do not fulfill all requirements for validation of simulation tools for NASA missions of interest for two reasons. First, while test data were obtained in reacting CO_2 environments, the enthalpy levels were lower than the range of conditions obtained in the first phase of this test program (on the MSL geometry) and chemical kinetics did not have a major influence on heating levels. Second, these data were obtained on a sharp cone model, not on a blunt body configuration that would be relevant to entry vehicle design. Therefore, while the results of this study provide some measure of confidence in the performance of computational tools, no definitive conclusions can be made as to the fidelity of these models for realistic entry vehicle design at Mars-relevant conditions and further research in this area is warranted.

VI. Acknowledgements

This work was supported by the NASA Entry Systems Modeling Project of the Game Changing Development Program and through the NASA Space Technology Research Grants Program, grant # NNX12AG48A.

VII. References

1. Goodliff, K., Cirillo, W., Mattfeld, B., Stromgren, C., and Shyface, H., "Comparison of Human Exploration Architecture and Campaign Approaches," AIAA Paper 2015-4413, AIAA SPACE 2015 Conference and Exposition, Pasadena, CA, August 31 – September 2, 2015.

2. Craig, D. A., Troutman, P., and Herrmann, N. B., "Pioneering Space Through an Evolvable Mars Campaign," AIAA Paper 2015-4409, AIAA SPACE 2015 Conference and Exposition, Pasadena, CA, August 31 – September 2, 2015.

3. Dwyer Cianciolo, A. M., Davis, J. L., Komar, D. R., Munk, M. M., et al, "Entry, Descent and Landing Systems Analysis Study: Phase 1 Report," NASA TM-2010-216720, July 2010.

4. Dwyer Cianciolo, A. M., Davis, J. L., Engelund, W. C., Komar, D. R., et al, "Entry, Descent and Landing Systems Analysis Study: Phase 2 Report," NASA TM-2011-217055, February, 2011.

5. Edquist, K. T., Dyakonov, A. A., Wright, M. J., and Tang, C. Y., "Aerothermodynamic Design of the Mars Science Laboratory Heatshield," AIAA Paper 2009-4075, 41st AIAA Thermophysics Conference, San Antonio, TX, June 22-25, 2009.

6. Way, D. W., "Preliminary Assessment of the Mars Science Laboratory Entry, Descent and Landing, Simulation," IEEEAC Paper 2755, 2013 IEEE Aerospace Conference, Big Sky, MT, March 2-9, 2013.

7. Edquist, K. T., Hollis, B. R., Johnston, C. O., Bose, D., White, T. R., and Mahzari, M., "Mars Science Laboratory Heat Shield Aerothermodynamics: Design and Reconstruction," *Journal of Spacecraft and Rockets*, Vol. 51, No. 4, July-August 2014, pp. 1106-1124.

8. Hollis, B. R. and Prabhu, D. K. "Assessment of Laminar, Convective Aeroheating Prediction Uncertainties for Mars-Entry Vehicles," *Journal of Spacecraft and Rockets*, Vol. 50, No. 1., January-February 2013, pp. 56-68.

9. MacLean, M., Dufrene, A., Carr, Z., Parker, R. and Holden, M., "Measurements and Analysis of Mars Entry, Descent and Landing Aerothermodynamics at Flight-Duplicated Enthalpies in LENS-XX Expansion Tunnel," AIAA Paper 2015-1897, AIAA SciTech Conference, Kissimmee, FL, January 5-9, 2015.

10. Hollis, B. R., Prabhu, D. K., Maclean, M. and Dufrene, A., "Blunt-Body Aerothermodynamic Database from High-Enthalpy CO_2 Testing in an Expansion Tunnel," AIAA Paper 2016-4151, 46th AIAA Thermophysics Conference, Washington, D.C., June 13-17, 2016.

11. Hollis, B. R., Prabhu, D. K., Maclean, M. and Dufrene, A., "Blunt-Body Aerothermodynamic Database from High-Enthalpy Carbon-Dioxide Testing in an Expansion Tunnel," *Journal of Thermophysics and Heat Transfer*, Vol. 31, No. 3, July-September 2017, pp. 712-731.

12. Dufrene, A., MacLean, M., Parker, R., Wadhams, T., and Holden, M., "Characterization of the New LENS Expansion Tunnel Facility," AIAA Paper 2010-1564, 48th AIAA Aerospace Sciences Meeting & Exhibit, Orlando, FL, January 4-7, 2010.

13. Dufrene, A., MacLean, M., and Holden, M., "Experimental Characterization of the LENS Expansion Tunnel Facility Including Blunt Body Surface Heating," AIAA Paper 2011-0626, 49th AIAA Aerospace Sciences Meeting, Orlando, FL, January 4-7, 2011.

14. MacLean, M., Dufrene, A., and Holden, M., "Spherical Capsule Heating in High Enthalpy Carbon Dioxide in LENS-XX Expansion Tunnel," AIAA Paper 2013-0906, 51st AIAA Aerosciences Meeting, Grapevine, TX, January 7-10, 2013.

15. MacLean, M., Dufrene, A., Wadhams, T., and Holden, M., "Numerical and Experimental Characterization of High Enthalpy Flow in an Expansion Tunnel Facility," AIAA Paper 2010-1562, 48th AIAA Aerospace Sciences Meeting & Exhibit, Orlando, FL, January 4-7, 2010.

16. Marineau, E. C., Lewis, D. R., Smith, M. S., Lafferty, J. F., White, M. E., and Amar. A. J., "Investigation of Hypersonic Laminar Augmentation in the Stagnation Region," AIAA Paper 2013-0308, 51st AIAA Aerospace Sciences Meeting, Grapevine, TX, January 7-10, 2013.

17. Mazaheri, A., Gnoffo, P. A., Johnston, C. O. and Kleb, W. L., "LAURA Users Manual: 5.5-65135," NASA TM-2013-217800, February 2013.

18. Wright, M. W., White, T. and Mangini, N., "Data Parallel Line Relaxation (DPLR) Code User Manual Acadia – Version 4.01.1," NASA TM-2009-215388, October 2009.

19. Baldwin, B. S. and Lomax, H., "Thin Layer Approximation and Algebraic Model for Separated Turbulent Flows," AIAA Paper 1978-0257, AIAA 16th Aerospace Sciences Meeting, Huntsville, AL, January 16-18, 1978.

20. Cebeci, T. and Smith, A. M. O., "Calculation of Compressible Adiabatic Turbulent Boundary Layers," AIAA Paper 1969-0687, AIAA Fluid and Plasma Dynamics Conference, San Francisco, CA, June 16-18, 1969.

21. Spalart, P. R. and Allmaras, S. R.," A One-Equation Turbulence Model for Aerodynamic Flows, *Recherche Aerospatiale*, No. 1, 1994, pp. 5-21.

Catris, S. and Aupoix, B., "Density Corrections for Turbulence Models," Aerospace Science and Technology, Vol. 4, 2000, pp. 1-11.

22. Wilcox, D. C., "Formulation of the *k*-ω Turbulence Model Revisited," *AIAA Journal*, Vol. 46, No. 11, November 2008, pp. 2823-2838.

23. Hollis, B. R., Horvath, T. J., Berger, K. T., Lillard, R. P., Kirk, B. S., Coblish, J. J., and Norris, J. D., "Experimental Investigation of Project Orion Crew Exploration Vehicle Aeroheating in AEDC Tunnel 9," NASA TP-2008-215547, December 2008.

24. Hollis, B. R. and Collier, A. S., "Experimental Investigation of Mars Science Laboratory Entry Vehicle Aeroheating in AEDC Hypervelocity Tunnel 9," NASA TP-2017-219658, September 2017.

25. Dhawan, S. and Narasimha, R., "Some Properties of Boundary Layer Flow During the Transition from Laminar to Turbulent Motion," Journal of Fluid Mechanics, Vol. 3, No. 4, January 1958, pp. 418-436.

26. Edquist, K. T., Dyakonov, A. A., Wright, M. J., and Tang, C. Y., "Aerothermodynamics Environments Definition for the Mars Science Laboratory Entry Capsule," AIAA Paper 2007-1206, 45th AIAA Aerospace Sciences Meeting and Exhibit, Reno, NV, January 8-11, 2007.